A multi-scale study of the interaction of Sn solutes with dislocations during static recovery in α-Fe

N. Mavrikakis, C. Detlefs, P.K. Cook, M. Kutsal, A.P.C. Campos, Melanie Gauvin, P.R. Calvillo, W. Saikaly, R. Hubert, H.F. Poulsen, et al.

To cite this version:

N. Mavrikakis, C. Detlefs, P.K. Cook, M. Kutsal, A.P.C. Campos, et al.. A multi-scale study of the interaction of Sn solutes with dislocations during static recovery in α-Fe. Acta Materialia, 2019, 174, pp.92-104. 10.1016/j.actamat.2019.05.021 . hal-02403188

HAL Id: hal-02403188
https://hal.science/hal-02403188

Submitted on 14 Dec 2020

A multi-scale study of the interaction of Sn solutes with dislocations during static recovery in α-Fe

N. Mavrikakis[a,b], C. Detlefs[c], P.K. Cook[c], M. Kutsal[c,d], A.P.C. Campos[e], M. Gauvin[f], P.R. Calvillo[f], W. Saikaly[f], R. Hubert[f], H.F. Poulsen[d], A. Vaugeois[g], H. Zapolsky[g], D. Mangelinck[a], M. Dumont[a], C. Yildirim[c,f,*]

[a]*Aix-Marseille University, Institut Matériaux Microélectronique Nanosciences de Provence-IM2NP, UMR CNRS 7334, France*
[b]*ArcelorMittal Maizières Research SA, Voie Romaine, BP 30320, 57283, Maizières les Metz, France*
[c]*European Synchrotron Radiation Facility, 71 Avenue des Martyrs, CS40220, 38043 Grenoble Cedex 9, France.*
[d]*Department of Physics, Technical University of Denmark, 2800 Kgs. Lyngby, Denmark*
[e]*Aix Marseille Université, CNRS, Centrale Marseille, FSCM, CP2M, 13397, Marseille, France*
[f]*OCAS, Pres. J.F. Kennedylaan 3, BE-9060 Zelzate, Belgium*
[g]*GPM UMR 6634 CNRS, Université de Rouen, F-76801 Saint Etienne du Rouvray, France*

Abstract

The properties of engineering materials can be improved by optimising the microstructural developments during annealing processes. Here, we investigate the effect of Sn on the recovery annealing of cold rolled Fe-3%Si alloys. We use a multiscale approach combining micro hardness, electron back scattering diffraction (EBSD), and dark field X-ray microscopy (DFXM): a recent, non-destructive synchrotron-based technique that allows 3D mapping of orientation and lattice strain within individual grains embedded in bulk samples. Micro hardness results show that the Sn solute has a strong effect on the recovery kinetics. These results are compared to a physical kinetic model suggesting that Sn limits the softening. This observation is further discussed by a complementary atomistic modelling that demonstrates solute-dislocation interaction around edge dislocations. *In situ* DFXM experiments reveal the 3D microstructural evolution upon annealing at the grain level with high angular resolution. The DFXM observations show that Sn slows the recovery kinetics within individual grains, in agreement with the other microscopic investigations. Furthermore, the DFXM results provide a direct observation of strain fields around dislocation loops in an embedded single grain, which is argued to remain static due to solute effect during recovery.

Keywords:
ferrite, recovery, solute atom, dark field X-ray microscopy (DFXM), dislocation.

---

1. Introduction

Metal processing routes usually include steps of plastic deformation that assist in controlling the internal micro-structure, which is directly related to the final properties of the material. Cold deformation processes such as rolling, forging, drawing etc. introduce a high density of dislocations that is heterogeneously distributed within the crystalline structure. Typically, walls of dislocations separate near perfect subgrains. These deformation-induced dislocations result in hardening of the material, and constitute the main driving force for the annealing phenomena. Upon subsequent annealing, the material restores via processes known as recovery and recrystallisation. Recrystallisation can be defined as nucleation and growth of near perfect crystals and involves the migration of high-angle grain boundaries whereas recovery usually involves the re-arrangement and annihilation of dislocation dipoles, along with migration of low-angle grain boundaries [1]. Recovery can occur prior to and concurrent with recrystallisation. Since the driving force for both phenomena is the stored energy of deformation, the ease of recrystallisation will dictate the extent of recovery. Therefore, the understanding of these two competing phenomena is of significant industrial relevance.

Over the past decades, numerous studies focused notably on recrystallisation [2], while recovery has received comparably less attention. Recovery depends on several microstructural factors such as the amount of strain introduced during plastic deformation, the annealing temperature, and the crystal structure of the material [1], in particular, the stacking fault energy (γSFE). γSFE is associated with the extent of dissociation of unit dislocations into partials. Low γSFE corresponds to easy dissociation, hindering the dislocation motion within the lattice. For example, in Cu and austenitic stainless steels dislocation motion is difficult. On the other hand, for high γSFE metals (e.g. Al and α-Fe), dislocation motion is rapid, and extensive recovery may take place consuming a large part of the stored energy [3]. Another important factor affecting recovery is chemistry. Solute atoms may change γSFE either by pinning dislocations or by interacting with vacancies [4, 5, 6]. Such effects result in alterations in stress relaxation during annealing by modifying the available stored energy. In this respect, under-

---

[*] Corresponding Author
Email address: `can.yildirim@esrf.fr` (C. Yildirim)

standing how chemical segregation affects dislocation mobility during annealing is of special importance.

Here, we study the effect of Sn addition on the recovery of Fe-Si single-phase alloys. Si is one of the most important alloying elements for the steel industry; its addition it is commonly used for the fabrication of core materials in magnetic flux carrying devices [7]. Si is known for enhancing solid solution strengthening of iron [8], and is an important α-Fe stabilising element [9] as for contents above 2 wt.% the allotropic α–γ transformation is suppressed, resulting in a bcc crystal structure up to liquidus. Finally, Si addition to iron also increases significantly its γSFE, to values as high as 0.2 J/m^2 [10], thus the annealing behaviour of Si added steels is strongly modified with recovery being promoted at the expense of recrystallisation, compared to pure Fe [8]. Meanwhile, the effect of solute Sn in recovery of other metallic materials has been reported, mainly for fcc systems with studies on Cu-Sn alloys discussing the effect due to segregation on dislocations [11, 12, 13]. For instance, Song et al. [14] studied the pinning effect of Sn solutes on grain boundary dislocation dissociation in Al-Mg alloys. However, to our knowledge, no literature regarding the effect of Sn on recovery of α-Fe has been reported. Furthermore, the majority of research on the Fe-Si system investigated compositions with multiple alloying elements.

The Fe-Si system has been chosen to study recovery in binary and ternary compositions. The aim of this work is to investigate the Sn solute effect during static recovery in α-Fe using a multi-scale approach. We approached the solute assessment experimentally by evaluating the stress relaxation with microhardness measurements, while studying the local characteristics of the deformed state by means of electron back-scatter diffraction (EBSD). To discuss the recovery at the dislocation scale and to rationalise the experimental observations, we applied an established physical kinetic model and modified it to the needs of the present work [15, 16].

To improve the 3D understanding of the recovery process, we employed a recently developed synchrotron technique, dark field X-ray microscopy (DFXM) [17]. Unlike its electron based counterparts (i.e. EBSD, transmission electron microscopy - TEM), which require several sectioning processes or very thin samples [18], DFXM provides non-destructive *in situ* mapping of orientation and strain with sub-micron spatial resolution in deeply-embedded grains. In addition, DFXM offers a high angular resolution superior to that of EBSD and TEM, which enables probing ultra-fine networks in embedded grains [19] and eliminates the limitations of diffraction peak overlap [20]. Recently, similar synchrotron based diffraction techniques such as 3DXRD [21] and diffraction contrast tomography (DCT) [22] provided interesting results on the recrystallisation and growth of near perfect grains. However, these methods fail to fulfil the requirements of mapping dislocation networks in individual grains that are highly deformed, due to the peak overlap problem and insufficient spatial resolution. Thus, the above mentioned qualities of DFXM makes it a powerful tool to study solute-dislocation interaction during *in situ* annealing.

Finally, we further discuss solute segregation at dislocations using atomistic modelling results granted by a powerful simulation method, the quasi-particle approach (QA) [23, 24]. Our results provide a thorough insight into how Sn affects recovery at several length scales, and how it correlates to material behaviour.

2. Experimental

A binary Fe-3 wt.% Si and a ternary alloy with the addition of 0.1 wt. % Sn were studied. Both Si and Sn solutes are in solid solution, and the alloys are single-phase ferritic, due to the high Si content. The total amount of residuals was between 160–380 ppm weight, quantities which are assumed to be negligible. The materials were lab processed in ArcelorMittal Global R&D Gent, with a final cold rolling step at a Von Mises true strain of about $\epsilon = 2$. As-cold-rolled samples were machined into small rectangular samples with dimensions of $10 \times 5\,\mathrm{mm}^2$ using the spark erosion wire cutting method. The 10 mm side was aligned parallel to the transverse direction (TD), while the 5 mm side was positioned parallel to the rolling direction (RD). Subsequently, the as-cold-rolled materials were heat treated using a DIL805bD Bähr dilatometer. A thermocouple was welded to the middle of the sample to regulate the temperature. The heat-treatment consisted of a heating at a constant rate followed by isothermal holding at the desired temperature and quenching to room temperature by He gas flow in the dilatometer chamber, ensuring segregation free cooling. Microstructural analysis for homogeneity of the heat-treated area was performed at the RD-normal direction (ND) cross section beneath the thermocouple (avoiding the area directly affected by the weld). Finally, the sample underwent the typical preparation for metallography, including mechanical grinding, polishing with diamond suspensions and finished with fine polishing using colloidal silica suspension with particle size of $0.04\,\mu$m. The recovery kinetics prior to recrystallisation were investigated with micro-hardness measurements, after annealing at various temperatures (773–973 K). The annealing treatments were selected taking into account that pure Fe has a recrystallisation temperature, $T_{\mathrm{REX}} \approx 823\,\mathrm{K}$ [1]. On one hand, materials were treated isothermally for various holding times at temperatures: 773, 823 and 873 K after a heating step of 25 K/s (isothermal treatment). On the other hand, to have a global understanding of the solute effect during recovery phenomena, recovery concurrent to recrystallisation was also studied after annealing at 973 K. For this purpose, an interrupted, non-isothermal, heat-treatment to 973 K was applied. In the non-isothermal treatment materials were heated to 973 K with a heating step of 25 K/s and quenched at steps of 50 K (i.e. at 773, 823, 873 K etc.). In the temperature regime of 773–823 K, no recrystallisation is expected for the binary nor the ternary alloy. This was confirmed by optical microscopy (for both alloys) and by *in situ* synchrotron diffraction experiments upon isochronal heating of the ternary alloy up to 923 K (see the Supplementary Information). The treated materials were analysed with EBSD, data were split into RX and non-RX (recovering) microstructure and the geometrically necessary dislocation (GND) dislocation densities were calculated. Experimental results were compared to an established physical model accounting for the microstructural characteristics such as heterogeneous dislocation density distribution, the decreasing available stored energy, and solute addition.

2.1. EBSD

Orientation maps were collected using the electron backscatter diffraction (EBSD) technique in a Zeiss Gemini 500 field-emission gun scanning electron microscope (FEG-SEM) equipped with an EDAX Hikari Super acquisition system. EBSD scans were performed at 15 kV accelerating voltage, at a working distance of 13–15 mm, using step sizes ranging between 0.4 and 0.05 μm and covering surface areas of about $900 \times 300\,\mu\text{m}^2$. The post-processing was performed in the OIM Analysis platform by TSL. Reconstruction of subgrains and grains was performed by the following boundary conditions: *subgrains* were assumed to be bounded by mainly low-angle boundaries (LAGBs) $2^\circ \leq \omega \leq 15^\circ$, and occasionally also by some high-angle boundaries (HAGBs) $\omega \geq 15^\circ$, whereas *grains* should be only bounded by HAGBs. The GND density, ρ was estimated from the EBSD data as proposed by Hughes and Hansen [25] and previously used in similar studies [26, 27, 28]:

$$\rho = \frac{3 \cdot (1 - f_{\mathrm{HAGB}}) \cdot \bar{\omega}_{\mathrm{LAGB}}}{b \cdot d_0}, \tag{1}$$

where f_{HAGB} is the fraction of HAGBs, $\bar{\omega}_{\mathrm{LAGB}}$ the average misorientation of LAGBs in radians, d_0 the subgrain diameter and **b** the length of the Burgers vector, 0.248 nm. The dislocation density calculations were performed on EBSD data collected in the as deformed condition: (i) in the entire scan area and (ii) after performing data partitioning as a function of restored microstructure (recovered or recrystallised). The restoration products can be separated by imposing internal misorientation criteria within the subgrains and grains providing a measure of the internal stored energy. In this study, the grain average misorientation (GAM) criterion, which describes the average misorientation between measured neighbouring points within a grain, was used. In partially recrystallised samples, recrystallised (RX) grains were defined as the grains which are bounded by HAGBs, and which have a low internal misorientation (GAM ≤ 1.5°). In addition, a grain shape criterion was applied such that the RX grains defined as near equiaxed in shape (i.e. a grain aspect ratio criterion was applied, from 1:1 to maximum 1:3 for RX grains). After defining the RX grains, the remaining microstructure constitutes the non-recrystallised/recovering regions, which were treated as a function of orientation. A common orientation representation of the sample-crystal reference system, uses the Miller indices {hkl} for the crystal plane that is parallel to the ND of the sample and ⟨*uvw*⟩ for the crystal direction parallel to the RD [29], and is the one used in this manuscript to describe grain orientations.

2.2. Hardness

The Vickers micro-hardness (HV) tests were performed at the RD-ND cross-section of the materials to quantify the softening fraction during restoration. A relatively small applied load of 50 g was preferred, as it was more sensitive to microstructural features than higher ones (such as 200–500 g). At least 9 indentations were applied at each condition from which the average value was taken. HV measurements were performed at room temperature after the samples had been subject to various heat-treatments in the dilatometer.

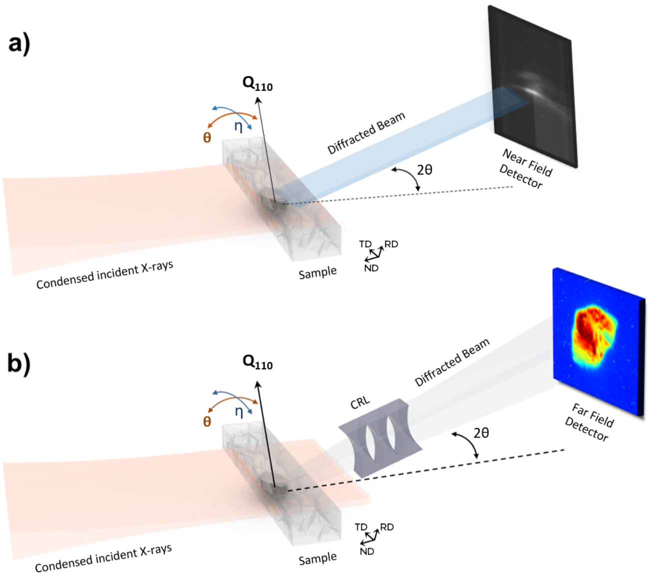

Figure 1: Schematic of the DFXM experimental setup. The angles θ, η, and 2θ correspond to the tilt angles around the Q_{110} scattering vector of the grain of interest (shown darker within the sample). The incident beam is focused vertically to illuminate about 1 μm slices of the grain. a) The near field diffraction without CRL, the diffraction ring is captured at about 40 mm distance from the sample. b) Microscopy set-up with an objective CRL placed along the diffracted beam to magnify the projection of the grain. The far field detector is at about 5 meters from the sample.

2.3. Dark Field X-ray Microscopy

Dark field X-ray microscopy (DFXM) is a full-field, non-destructive, and diffraction-based imaging technique for 3D mapping of orientation and strain of embedded grains in bulk materials. Unlike the bright-field imaging methods, the illumination comes from the Bragg diffraction of the sample, thus the image contrast is given by the diffracting crystal (i.e. grain). Fig. 1 shows the DFXM experimental set up. A selected grain in the near field geometry (Fig. 1a) is magnified by the compound refractive lenses (CRL) and projected to the far field (Fig. 1b).

The DFXM experiments were carried out at the beamline ID06 at the European Synchrotron Radiation Facility (ESRF). 17 keV photons were selected by a Si (111) Bragg-Bragg double crystal monochromator. The beam was pre-focused into the experimental hutch using a transfocator comprising 4 Be refractive lenses. Additionally, a compound refractive lens (CRL) comprising 58 1D Be lenses with 100 μm radius was used to focus the beam in vertical direction onto the sample at a focal distance of 75 cm to perform section topography. The beam profile on the sample was approximately $400 \times 1\,\mu\text{m}^2$ in horizontal and vertical directions, respectively. An indirect detector composed of a scintillator, optical microscope and a FReLoN CCD, with an effective pixel size of 1.24 μm and field-of-view of 2.5 mm was used as a nearfield imaging detector to align the sample and track the grains of interest, located 40 mm downstream of the sample. Located at 5345 mm from the sample, a similar indirect detector ("far field detector") with 1.4 μm effective pixel size imaged the (110) reflection of a grain in the interior. An X-ray objective lens with 88 Be parabolic lenslets, each with 50 μm apex radius was then positioned 278 mm from the sample along the Bragg beam, projecting a magnified image (magnification $M = 18.7$) onto the far field detector. The resulting effective and the numerical aperture (NA) were calculated as 273 μm and 0.5 mrad, respectively. This small numerical aperture led to high angular resolution in the three angular directions (θ, η, 2θ) [20]. The resolution for the sample rock ($\Delta\theta$) was given by the divergence of the 1D condenser CRLs while for the other two directions were given as $\Delta\eta = 2\mathrm{NA}/\sin(2\theta)$ and $\Delta 2\theta = 2\mathrm{NA}$, yielding 0.16° and 0.001°, respectively. Combining the optics of the far-field camera and the magnification the spatial resolution was determined to be $0.150 \times 0.394 \times 3\,\mu\mathrm{m}^3$ in the horizontal, vertical and depth directions.

To study recovery using DFXM, samples were cut to $0.170 \times 0.300 \times 8\,\mathrm{mm}^3$ size, at a 37° angle from the rolling direction, using spark erosion. Both the binary and ternary alloys were studied through different annealing steps following the same procedure. A grain with scattering vector Q_{110} approximately (within 7°) parallel to the vertical RD was selected for dark field imaging. In order to obtain 3D data of the diffracting grain, the sample was moved in the vertical direction to scan different 2D layers along the height of the grain. For each 2D layer, mosaicity and strain scans were recorded between different annealing steps. The former scan is a collection of images in two sample tilt axes (see Fig. 1), rocking and rolling, while the latter comprise a collective motion of the X-ray objective and the far-field detector through the Bragg angle 2θ. The mosaicity scans covered an angular range of the two-tilt axes between 0.8° to 0.4°, depending on the particular orientation distribution at different heating steps, with 0.02° per step. The strain scans were recorded in 21 and 24 steps over 0.14° and 0.24° in 2θ, respectively.

Isothermal heating experiments were conducted using a gas blower placed 10 mm from the sample. Several identical heating steps were performed to investigate the changes in the microstructure during recovery. Each heating step comprised an isothermal heating of the sample at 823 K for 11 minutes. Two heating steps for the binary and three for the ternary alloy were applied. Samples cooled down in air to room temperature.

3. Results

3.1. As Deformed State

The structure of the deformed state dictates the path for the recovery and recrystallisation phenomena that will take place in subsequent annealing treatments. Thus, it is important to have a comprehensive characterisation of the material at this stage. Deformed microstructures at large levels of strain are characterised by a well-defined network of subgrains forming a cellular structure in the grain interior [30]. Fig. 2a-b shows the EBSD ND inverse pole figure (IPF) superimposed on the image quality (IQ) mappings for the two alloys in the as deformed condition. Deformation features such as transition bands (i.e. shear bands, deformation bands) are present in both alloys, while an orientation dependence is observed. Dillamore et al. [31] found that the energy of deformation is stored heterogeneously within the different grain orientations, separating into regions with high and low stored energy density. In cold rolled bcc metals, high stored energy (HSE) orientations include the $\{111\}\langle uvw\rangle$ orientation (i.e. regions of high Taylor factor), while low stored energy orientations are centred near the $\{001\}\langle 110\rangle$ orientations [31, 32]. The $\{111\}\langle uvw\rangle$ grains, particularly the $\{111\}\langle 112\rangle$ component, form dense shear bands (Fig. 2a-b) crossing through these grains due to the higher slip activity of $\{111\}\langle 112\rangle$ to accommodate plastic deformation [33]. In contrast, the $\{001\}\langle 110\rangle$ orientation of the α-fibre contain relatively coarser subgrain structure and the lowest misorientations and thus, are low stored energy regions (LSE) [34, 35]. After cold rolling, the HSE regions are known to have higher tendency to recover [36] and

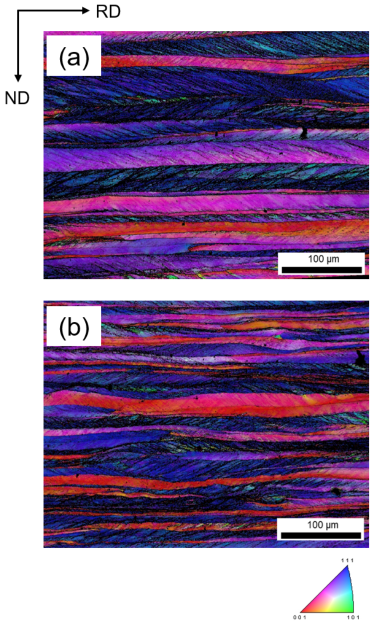

Figure 2: The overview of the microstructure in the as deformed state, the ND-IPF+IQ mappings as measured by EBSD for a) binary and b) ternary alloy.

Table 1: Microstructural data of the as deformed state from EBSD. The area fractions and estimated dislocation densities, ρ in $\times 10^{14}(m^{-2})$ from EBSD data as a function of orientation are shown for the binary and ternary alloys.

	Binary		Ternary	
Orientation	Area fraction	$\rho(m^{-2})$	Area fraction	$\rho(m^{-2})$
α -fibre	0.49	5.9	0.61	4.5
γ -fibre	0.39	9.6	0.38	8.5
$\{001\}\langle 110\rangle$	0.07	3.2	0.15	2.9
$\{112\}\langle 110\rangle$	0.09	5.9	0.07	8.0
$\{111\}\langle 110\rangle$	0.04	10.2	0.06	10.0
$\{111\}\langle 112\rangle$	0.06	11.9	0.07	10.8

recrystallise [2, 34] while LSE regions are more sluggish [34].

At this stage, both materials displayed strong rolling texture [37] – with a high intensity of the α-fibre ($\{hkl\}\langle 110\rangle$) and γ-fibre ($\{111\}\langle uvw\rangle$) orientations. The texture components and their corresponding intensities, in the as deformed state, were very similar for the two materials (Table 1). The EBSD data were used to estimate the dislocation densities, as a function of grain orientation in the as deformed state, listed in Table 1. The $\{111\}\langle 112\rangle$ and $\{001\}\langle 110\rangle$ orientations were found to have the highest and the lowest dislocation densities, respectively, in agreement with the observations of Dillamore et al. [31].

In an overview, the as deformed state of the two alloys have very similar estimated dislocation densities, in good agreement with the literature [30]. The complete EBSD characterisation of the deformed state shows no clear solute effect as far as the microstructural features, deformation texture, dislocation density and stored energy are concerned. Meanwhile, the heterogeneous nature of the deformed state can be observed within the samples; the rate of recovery is expected to be faster in orientations that have high dislocation density [36].

3.2. Evolution of Static Recovery

Recovery was studied with micro-hardness (HV) measurements to all materials, after performing isothermal and non-isothermal heat-treatments. The corresponding amount of recovery at a given time, H_t can be determined by calculating the fraction softened, R, [38] once the hardness values of the as deformed, H_0 and fully RX states, H_{FR} are known. R is then expressed as:

$$R = \frac{H_0 - H_t}{H_0 - H_{\mathrm{FR}}} \qquad (2)$$

Recovery data are often represented in fraction of residual strain hardening, $1 - R$, with the as deformed condition equal to unity. Hardness values can be correlated to the flow stress by using the empirical equation proposed by Busby et al. [39] based on experimental observations in ferritic steels compiling data found in literature. According to these authors, the yield stress correlates with hardness values with a factor of $\sigma = 3.06 \cdot \mathrm{HV}$.

The flow stress, σ relates to the total dislocation density, ρ, and the flow stress of the fully RX state, σ_{FR}, by the forest type hardening Taylor relationship [40]

$$\sigma = \sigma_{FR} + M\alpha G b\sqrt{\rho}, \qquad (3)$$

where M is the Taylor factor and α is the dislocation-dislocation junction strength affected by solute addition [41]. If the stress relaxation is assumed to occur controlled by thermally activated mechanisms, then the stress relaxation during recovery has a logarithmic decay with annealing time of the form:

$$\sigma = \sigma_0 - \frac{kT}{V_\alpha}\ln\left(1 + \frac{t}{t_0}\right), \qquad (4)$$

where σ_0 is the stress at $t = 0$ (i.e. as deformed), V_α being the activation volume for recovery events and t_0 is a reference time [1, 3, 42, 43]. In this description, the activation energy for thermally activated processes is a function of internal stress and it decreases with increasing dislocation density (i.e. cold strain), while increases with annealing time [1]. The logarithmic decay (Eq. 4) agrees very well with our experimental data to describe the recovery kinetics for both the binary and ternary alloy.

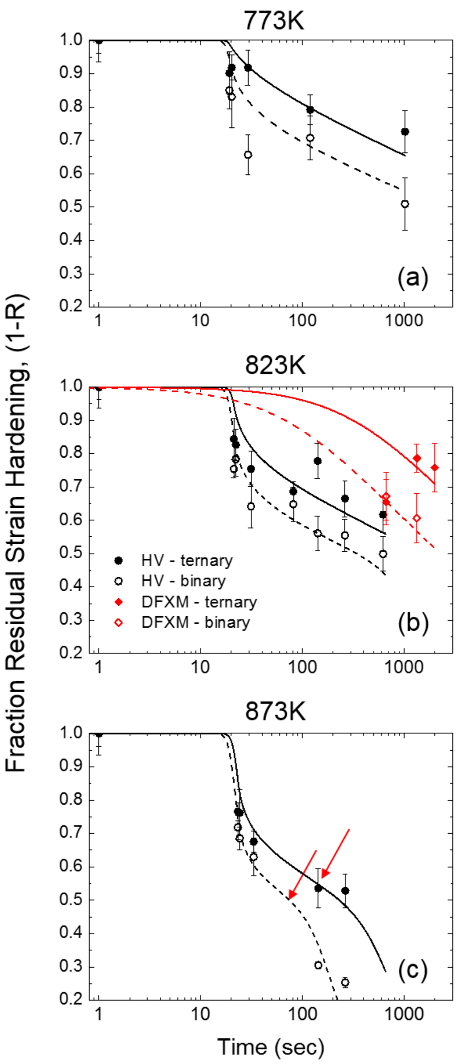

Figure 3: Fraction of residual strain hardening, $1 - R$ with annealing time during recovery prior to recrystallisation. Micro-hardness results for binary (open points/dashed lines) and ternary (solid points/lines) alloys after annealing at a) 773 K, b) 823 K in comparison to DFXM data and c) 873 K. The fit was done using Eq. 6.

3.2.1. Recovery Prior to Recrystallisation

The fraction of residual strain hardening with annealing time for the isothermal annealing is shown in Fig. 3 for the two alloys for a) 773, b) 823 and c) 873 K. The experimental data clearly show that the addition of Sn solute reduces the stress relaxation after similar annealing times, as the ternary alloys exhibit slower recovery kinetics compared to the binary alloys. Moreover, the onset of recrystallisation is observed when the annealing time is longer than 100 seconds at 873 K. The DFXM and the fitting of the experimental data will be discussed in subsequent sections.

3.2.2. *Single-Grain Study of Recovery*

After having investigated recovery at the microscopic level, we now turn to evaluate the recovery in individual grains. In an effort to establish an understanding of recovery at the nanometer scale, we studied one embedded grain for each alloy using DFXM and traced their structural evolution upon annealing. For the binary alloy, the length of the grain along TD was about 5 μm and the height was scanned in 6 layers over 12 μm. For the ternary alloy grain, the length along TD was about 10 μm and the height was scanned in 8 layers over 20 μm. In the following we refer to these grains as grain B and grain T, respectively. To ensure the optimum signal-to-noise ratio for the DFXM experiment, the grains studied had similar orientation, belonging to a LSE region of the as deformed structure.

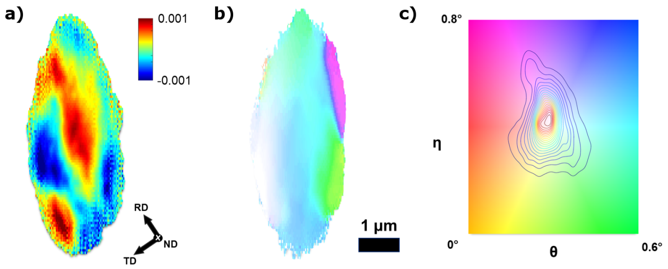

Figure 4: Reconstructed cross-sectional dark field X-ray microscopy maps of an embedded grain of the binary alloy, a) strain and b) lattice orientation. c) colour key showing the local orientation (θ, η) with an overlaid contour map of the integrated intensity distribution

Fig. 4 shows an example of the reconstructed magnified real-space maps of a layer of grain B after 22 minutes of annealing at 823 K. In Fig. 4a, a reconstructed strain map is shown, revealing the deviations from the nominal scattering angle 2θ at which the intensity of the grain is the highest. The high angular resolution given by the objective CRLs can unveil the finest details of different strain regions. These regions comprise compressive and tensile states within the layer. This kind of opposite signed strain bands are observed in almost all the layers of the grains studied for the binary and the ternary alloy. It can be argued that these bands may be shear or micro-bands formed due to cold rolling. Similar results were found in DFXM studies on other grains that were oriented differently with respect to the ND (not shown here). Fig. 4b shows the local orientation of 110 plane normal. This may be interpreted as part of the (110) pole figure to better understand the orientation map. These types of orientation (mosaicity) maps that are similar to that of EBSD are obtained by scanning the sample tilts (θ, η). Each raw image represents combination of these tilts around the 110 scattering vector. A detailed explanation of the DFXM data reconstruction is given elsewhere [44]. The mosaicity map shows regions with different orientation, revealing the subgrain structure during the course of recovery. Fig. 4c shows the local orientation color key and the overlaid integrated intensity distribution contour plot.

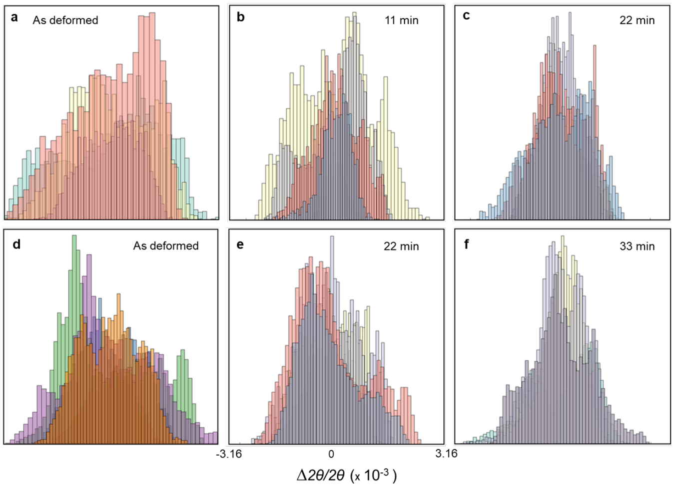

Figure 5: Histograms showing the relative axial strain distribution upon annealing for the binary (a-c) and the ternary alloy (d-f). Colours in each graph represents different layers of the grains. The colour coding is merely a selection of representation

We applied the same reconstruction algorithms as in Fig. 4 to the acquired data of the different layers to generate mosaicity and strain maps. Fig. 5 shows a comparison of the evolution of strain distribution upon different annealing stages. These plots are generated from the relative strain center-of-mass maps of each layer. It is seen that in the as deformed state, strain levels are on the order of 10^{-3} for both grains. Furthermore, in the as deformed state, grain B has a higher spread of internal strain compared to grain T. This may simply be due to statistical reasons as both grains were oriented in the same way. Another reason could be due to the size differences of the two grains. Furthermore, the strain distribution over the height of the both grains are quite inhomogeneous at the initial state. Upon annealing, the average full width at half maximum (FWHM) values of the layers decrease for both grains, indicating a more homogenous strain distribution in 3D as the grains recover. However, an interesting outcome can be seen when grain B and grain T are compared at different annealing stages. For grain B, the average FWHM values of different layers at 11 minutes and at 22 minutes are $(7 \pm 0.5) \cdot 10^{-4}$ and $(4.5 \pm 0.5) \cdot 10^{-4}$, respectively. The overall strain relaxation is about 36 % at the end of 22 minutes of annealing. For grain T, however, similar FWHM values are only obtained after annealing for an additional 11 minutes. This finding coheres well with the micro-hardness results, which show that the ternary alloy recovers more slowly. Therefore, one can speculate that, regardless of the higher initial strain level of grain B, the solute effect in grain T results in at least 50 % longer relaxation times of the internal stresses.

A direct comparison of the recovery kinetics at 823K from HV and DFXM data (taking the mean strain values of all layers) is shown in Fig. 3b. The decrease in $1 - R$ with time from DFXM data is following the tendency observed in microhardness, however the kinetics obtained from DFXM were slower. We shall note at this point that we studied the grains with one of the most intense signal in both samples. The outcomes of this choice are two-fold; firstly, the grains gave good signal to noise ratio, which led to smaller exposure times, and secondly, we studied supposedly one of the least-deformed grains within the entire sample (LSE). This assumption can explain the relatively slower kinetics observed in DFXM compared to the micro-hardness at 823 K (Fig. 3b), as LSE regions are expected to exhibit slower kinetics in restoration. Nevertheless, the solute effect that was observed in the least-deformed grains should be even more prominent in the highly deformed regions such as γ- and high Φ Euler angle α-fibre.

3.2.3. Recovery Concurrent to Recrystallisation

The recovery concurrent to recrystallisation was studied with EBSD after data partitioning. The dislocation density was calculated for the recovering regions (non-RX) during the progress of recrystallisation as a function of grain orientation.

Fig. 6a–b shows the decay with time of the dislocation density (calculated with Eq. 1) from EBSD. The calculated data were fitted with the thermally activated logarithmic decay relationship (Eq. 4). Assuming that Sn solutes impede the dislocation motion during recovery, then the decay time should be affected. This is indeed observed even in the overall material behaviour (black lines Fig. 6). However, more insight into the recovery mechanisms can be gained by investigating the stress relaxation within individual grains, as even in a solute-free material the processes vary with orientation — mostly due to differences in the initial dislocation density. For the binary alloy (Fig. 6a) the γ-fibre regions, as expected, show a faster decrease in dislocation density during recovery. In fact, γ-fibre regions reach almost full recrystallisation for an overall RX fraction of 0.5 (few γ-fibre recovering regions remain). By contrast, in the ternary alloy, such behaviour is not observed (Fig. 6b); the dislocation density within the γ-fibre regions is fairly stable with annealing time. The observed effect of the Sn solute on the recovery of other orientations (i.e. α-fibre, $\{001\}\langle110\rangle$) components is weaker. We shall discuss this observation further in paragraph 4.2.

3.3. Modelling the Segregation at Dislocations

To understand the solute segregation behaviour in Fe-Sn systems at atomic level, we used the recently-proposed quasi-particle approach (QA) [24]. This method was already applied to study the grain boundary structures in α-Fe and vacancy annihilation at grain boundaries [23, 45]. QA is based on the atomic density function theory (AFT) introduced by Khachaturyan [46] where they studied the order-disorder phase transformation at the rigid Ising lattice. In this method, we assume that each atom is a sphere comprising finite elements which are atomic fragments. We treat these fragments as pseudo-particles which are named fratons. We consider the fratons as interacting pseudo-particles occupying sites of the computational grid playing a role of the underlying Ising lattice. The proper choice of a model Hamiltonian describing the interaction of fratons should result in both their ”condensation” into atomic spheres and the movement of the spheres into the desirable equilibrium atomic configuration driven by the spontaneous minimization

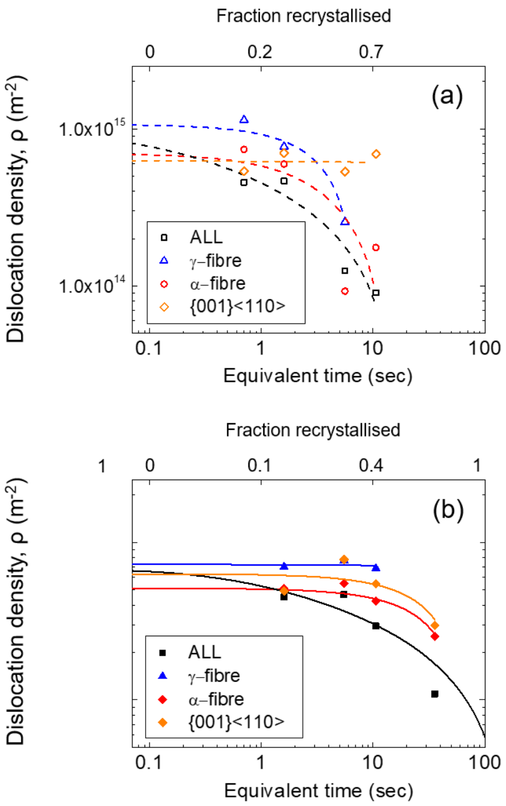

Figure 6: The evolution of dislocation density with annealing time during recovery concurrent to recrystallisation at 973 K. The EBSD calculated values as a function of grain orientation for a) the binary (open points/dashed lines) and b) the ternary alloy (solid points/lines).

of the free energy. The evolution of the density function of the fratons of specie α, $\rho_\alpha(\mathbf{r})$, is described by the microscopic diffusion equation :

$$\frac{d\rho_\alpha(\mathbf{r})}{dt} = \sum_{\mathbf{r}'}\sum_{\beta=1}^{\beta=m} \frac{L_{\alpha\beta}(\mathbf{r}-\mathbf{r}')}{k_B T}\frac{\delta G}{\delta\rho_\beta(\mathbf{r}',t)} \qquad (5)$$

where $L(\mathbf{r})_{\alpha\beta}$ is the matrix of kinetic coefficients, $\rho_\alpha(\mathbf{r},t)$ is the occupation probability of finding a fraton of the kind α (α = 1, 2, ..., m) at the site $\mathbf{r}$, m is the number of components, k_B is the Boltzmann constant, T and G are temperature and the non-equilibrium Gibbs free energy, respectively (see the Supplementary Information).

Equation 5 was solved using a Fourier-spectral method where the fraton interaction potentials are given as a sum of short-range and long-range contributions, while the mean field expression was used for the free energy. In the case of Fe-Sn, the parameters of the potential were chosen to reproduce the BCC crystal structure of this system and the misfit produced by the difference in the atomic sizes of Fe and Sn atoms within a simulation box typically of 2 x 10 x 10 nm^3. More information on the simulation details and parameters is given in the Supplementary Material.

In the binary Fe-Sn system assumed here, QA relies on the atomic misfit created in the lattice by the presence of a solute.

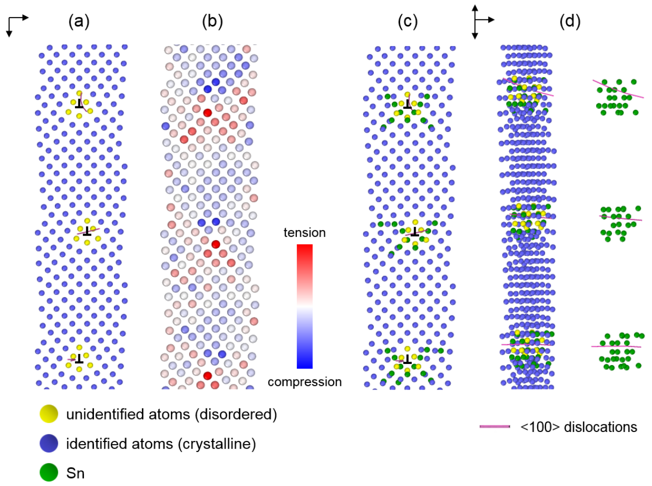

Figure 7: Solute Sn adsorption at edge $\langle 100\rangle$ dislocations in a low-angle dislocation boundary, the dislocation configuration after DXA analysis is shown. a) Fe atoms occupying lattice sites are shown in blue while disordered atoms around defects in yellow – dislocations lines are also shown, b) the elastic field within the crystal lattice and c-d) shows the segregation of Sn atoms (green) forming Cottrell atmospheres at dislocation lines.

Thus, the elastic energy created by this atomic misfit is the driving force for solute diffusion towards a lower energy configuration. In this context, QA in several cases predicted the segregation of Sn atoms at different dislocation configurations. A dislocation analysis was performed in the simulation results, using the Dislocation Extraction Algorithm (DXA), a computational method developed by Stukowski et al. included in the visualisation package OVITO [47, 48]. DXA assisted in identifying all dislocations within the crystal and determining their Burgers vectors, drawing a line representation for each dislocation. An indicative case of solute adsorption at $\langle 100\rangle$ edge dislocations at a LAGB, $\theta = 7.15°$ is shown in Fig. 7.

In this configuration, blue and yellow spheres, represent Fe atoms of the lattice that are in the expected sites and disordered atoms due to the presence of a crystal defect, respectively. Sn atoms (green spheres) were observed to segregate at dislocations creating Cottrell atmospheres around them, Fig. 7d. QA approach, also predicted the solute adsorption of Sn at $^1/_2\langle 111\rangle$, $\langle 100\rangle$ and $\langle 110\rangle$ dislocations within the simulation results. The Cottrell atmospheres at dislocations are directly related with the elastic field. The elastic field in the Fe lattice was calculated using the Voronoi cell. The Voronoi cell is defined as the part of the space situated closer to a given atom than to any other one. Thus, the relative deviation of the local atomic density from its bulk value reflects the local strain (compression-expansion) field. Fig 7 shows the elastic field in the Fe lattice in the proximity of the LAGB, red and blue atoms represent the zones under tension and under compression respectively. A comparison with Fig. 7b-c shows that Sn atoms preferentially occupy the following sites: (i) close to the maximum tensile zones and (ii) at the boundary between the tensile-compression zones. In contrast, no Sn atoms are observed at the zone of maximum compression.

4. Discussion

In the view of our multi-scale results, the general picture reveals that Sn solutes slow down the recovery process in Fe-Si system. On the one hand, the EBSD data allowed the estimation of dislocation density as a function of grain orientation; it was shown that solutes may affect more the HSE than LSE regions during *concurrent recrystallisation*, probably a result of higher dislocation density in HSE regions (Fig. 6). On the other hand, turning to recovery of embedded grains, DFXM results showed that the stress relaxation during *prior recovery*, even in the LSE regions are clearly affected by solute addition (Fig. 5).

The Sn interaction with dislocation configurations can be understood by the simple model example using the atomistic QA method, where Sn atoms were observed to create Cottrell (solute) atmospheres around the dislocation cores of edge dislocations [49]. For the case of thermally activated dislocation motion in a solute-free material, dislocations start to rearrange into lower energy configurations during recovery. They create pile-ups and accumulate at subgrain boundaries or annihilate with dislocations of the opposite sign. However, in the presence of solute atoms, and when the relaxation time for a solute to occupy a jog site is shorter than the time required for solute to break-away from the dislocation, the glide of the dislocation is controlled by thermal activation of the solute [50]. Solute atoms are considered to affect recovery via solute drag effect on dislocation motion [51]. The solute segregation around dislocation cores pins dislocations, making them sessile and a high driving pressure is then required for the dislocations to escape from the solute environment [52, 53, 54, 55, 56]. Takeuchi et al. [57] and Nabarro [58] theoretically treated the solute drag effect on a climbing and a gliding dislocation. They found that for the same velocity of dislocation motion, the effect is of similar order for the two cases. Tapasa et al. reported that Cu solutes pinned dislocation glide; and noted that at lower temperatures, edge dislocations glide faster than screw [52]. More recently, Hanlumyuang et al. showed that C solutes accumulated at tensile regions of $\{111\}\langle 1\bar{1}0\rangle$ edge dislocations, while they observed less segregation at a $^1/_2\{111\}\langle 1\bar{1}2\rangle$ screw component [59]. Solute segregation at dislocations and dislocation intersections (such as jogs) influences the activation enthalpy, activation volume for recovery [60] but also can reduce the dislocation formation energy [61]. One of the early studies on experimental observation of Cottrell atmospheres at an edge dislocation has been reported in an ordered Fe-Al alloy doped with B by Blavette et al from atom probe tomography (APT) results [62]. More recent studies with APT have followed, observing solute atmospheres of Nb, B and C at edge dislocations [63, 64] whereas also Si, Ni and P were found at the cores of screw dislocations [65].

4.1. Direct observation of solute dislocation interaction in situ

We now turn to our DFXM results to investigate the interaction of Sn solute with dislocations during the *prior recovery*. The grain resolved recovery study with DFXM gives access to a unique observation of intragranular defect arrangement. Local orientation differences (misorientation) can be ex-

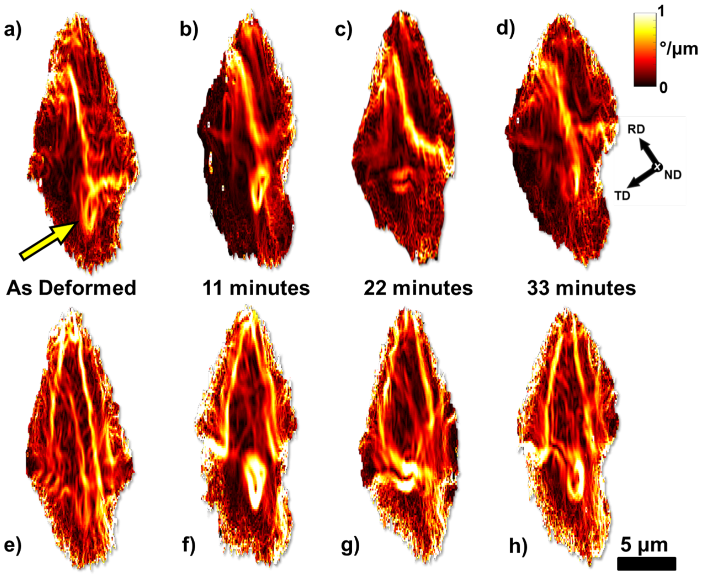

Figure 8: Radial gradients of the local orientation θ (a-d) and η (e-h) of a layer of grain T during recovery at 823 K.

tracted from the mosaicity scans with remarkable angular resolution [19, 66]. The angular resolutions of the DFXM results are $\Delta\theta = 0.015°$ and $\Delta\eta = 0.16°$. From the mosaicity scans, the mean local orientation difference between neighbouring voxels can be calculated by $\Delta\omega = \sqrt{(\Delta\theta)^2 + (\Delta\eta)^2}$. Sensitive intragranular defect features of dislocation arrangements can be observed by plotting the local orientation gradient of the tilt angles θ and η for neighbouring voxels within each layer. Fig. 8 shows the radial orientation gradient in the two directions, (a-d) in the tilt angle θ and (e-h) in the tilt angle η, for a corresponding layer in grain T after each annealing step. The orientation gradient in grain T reveals the intra-granular defect configuration with small, spaghetti-like formations, which correspond to the dislocation structures and their strain fields in the grain interior. It is observed that during annealing the more chaotic arrangement of the initial state is shifting into a smoother and well-defined network via recovery phenomena. In addition, lines of higher misorientation are observed in both gradient maps, crossing the grain interior diagonally. Inside the same grain a linear feature and a small loop are observed, the whole complex resembles a dislocation ensemble caused by the intersection of a line and a loop dislocation [67], and will be so forth referred to as dislocation complex. This dislocation complex in grain T, is a very interesting feature, as it can be a direct observation of intersecting dislocation lines and dislocation loops (or the strain field caused by them) in an embedded grain. Dislocation loops can form by the motion of dislocations with jogs during yielding and straining [49] and might play a crucial role in the metals performance, as for instance in irradiated steels [68, 69].

Loop diameter is expected to vary. Wei and Baker observed dislocation loops ranging from 10 to 100 nm that formed loop arrays in fatigue loaded pure Fe charactarized by TEM [70]. Moreover, in another study, Gemperle observed dislocation arrangements and loop formation in deformed Fe-3.2% Si bicrystals spreading along 0.5–1 μm in length [71].

DFXM experiments may prove to be inefficient to detect single dislocations due to the current spatial resolution. Nevertheless, the strain field around a dislocation can create enough angular spread to magnify the effect of the dislocations on the surrounding lattice such that DFXM can resolve. Moreover, the possibility that the observation consists of arrays of several dislocations together should also be considered. If solute atoms were pinning a jog, strain induced motion during cold work of other dislocations may as well get pinned at the site.

Another interesting feature of Fig. 8 is that the dislocation complex is still visible after different annealing steps, although its overall misorientation has decreased and it seems like it has dissociated into its individual constituents, lines and loops (Fig. 8b,f). The loop is even more visible in the η-gradient plot (Fig. 8e-h). The further heat-treatments seem to contribute in decreasing the local high misorientation regions, but the variance is not that profound. Terentyev et al. studied in detail the solute segregation (of Cr and Mn) effect on dislocation loop motion in irradiated steels, based on Monte Carlo simulations [68, 72]. The mobility and the interaction mechanism of ${}^{1}/_{2}\langle 111\rangle$ loops with the solutes differed greatly, compared to the pure iron reference material, enhancing the hardening of these steels. According to these authors [68, 72], the main elements of such interaction, in the presence of Cr solutes, are the following: 1) the edge dislocation gets attracted to the loop, 2) dislocation glide is hindered by the pinning effect of solutes and 3) an increased critical resolved shear stress is needed to unpin the dislocation loop from the solute atmosphere.

From the experimental results and the observation of the dislocation complex it is assumed that a similar scenario with Sn solute pinning dislocation glide may be acting, although the mechanism is more challenging to be obtained by a true step-by-step experimental observation. Other modelling studies also showed that dislocation loops become sessile in the presence of solutes [73], the binding energy of solute-dislocation will vary according to the solute-matrix atomic misfit. For Sn solutes in α-Fe Faulkner et al. calculated a binding energy value of $E_b^{\text{dis}} = -0.43\,\text{eV}$ that suggests that there is a high attractive force for Sn atoms to segregate at the dislocation core [74]. Meanwhile, solute-vacancy complexes may also be considered as possible dislocation traps as Terentyev et al showed for C-vacancy complexes [75].

Unfortunately, such a dislocation complex interaction was not observed in the grain of the binary alloy that was examined with DFXM. Nevertheless, it is believed that the stages would be similar to the ones described by Terentyev for the case of pure Fe, where the dislocation is more mobile and glides past the loop faster. The observation of a slower interaction in the ternary alloy is related to the dislocation being sessile due to solute pinning.

4.2. *Kinetic model*

To investigate the relation to the behaviour of the dislocations more closely, a modified approach for stress relaxation has been evaluated [15, 16, 42]. This approach is based on Friedel's description [42], which assumes recovery as a relaxation process of the internal stresses induced by the plastic strain, ϵ. Verdier et al. [15] then developed the model including the contribution of the varying dislocation density, $(\sigma - \sigma_{FR})^2$, during stress relaxation and providing a more detailed description of the activation parameters. In this approach, the rate of internal stress is expressed as [15]:

$$\frac{\mathrm{d}(\sigma - \sigma_{FR})}{\mathrm{d}t} = -\frac{64(\sigma - \sigma_{FR})^2 \nu_d}{9M^3\alpha^2 E} \exp\left(\frac{-U_\alpha}{kT}\right) \sinh\left(\frac{(\sigma - \sigma_{FR})V_\alpha}{kT}\right), \quad (6)$$

where U_α is the activation energy, of the recovery process, ν_d the Debye frequency and E the Young modulus. This recovery model incorporates the decrease in dislocation density of the non-RX structure at each step and calculates the residual driving force for recovery and subsequent recrystallisation. The version of the model used here is part of a kinetic model that couples recovery and recrystallisation proposed by Zurob et al. accounting for solute drag [16]. In the present work, we differentiate the model by taking into account the heterogeneous distribution of stored energy associated to dislocation density [78]. The microstructure was divided into HSE regions and LSE regions, macrotexture observations yielded the presence of HSE and LSE regions in the deformed state at a ratio of about 1. The kinetic model (Eq. 6), has been fitted numerically to the experimental data with the set of input parameters used listed in Table 2. For the ternary alloy, the addition of the solute contribution can be introduced in the dislocation-dislocation junction strength (α parameter), U_α or V_α. Mainly the α value was used to fit the experimental data as it has a direct physical link to dislocation motion [13, 41]. Nevertheless the U_α was also used as a secondary fitting parameter, while the V_α was considered to be independent of composition [60].

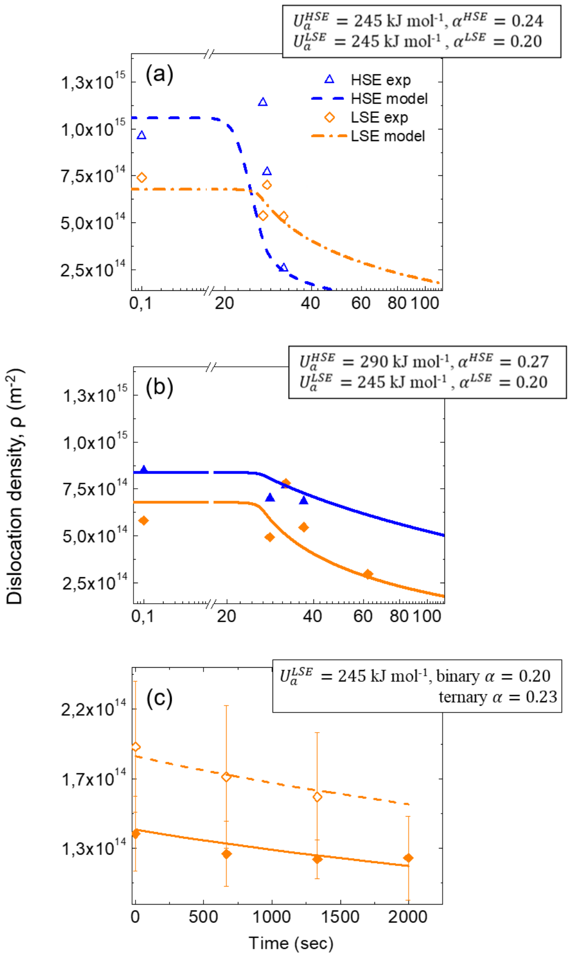

Figure 9: The predicted evolution of dislocation density with annealing time by Eq. 6 in comparison to the experimental data in high stored energy (HSE - blue) and low stored energy (LSE - orange) regions. The calculated dislocation density values (a,b) from EBSD data during recovery concurrent to recrystallisation at 973 K for binary and ternary alloy respectively, c) from DFXM data during prior recovery at 823 K in single grains fitted to Eq. 6 for the LSE regions for binary (open points/dashed lines) and ternary (solid points/lines) alloys.

The result of the fit to the experimental data is shown in Fig. 3a-c; the stress relaxation during recovery (prior and concurrent to recrystallisation) was reproduced with a good agreement to the HV and DFXM data. For annealing at 873 K, the model successfully predicted the onset of recrystallisation in the form of a narrow change in slope in the fraction softened (designated by red arrows in Fig. 3c), which was confirmed by optical microscopy observations.

In Fig. 9a–b we show the decay of the dislocation density due to *concurrent recovery* estimated from the EBSD data in HSE and LSE regions and predicted by the kinetic model. The shape of the curve depends on both the initial dislocation density and the dislocation-dislocation junction strength, α, while the ease of recovery initiation is depicted in the U_α. Solute addition resulted in an increase of the α and U_α values from 0.24 and 245 kJ mol^{-1} to 0.27 and 290 kJ mol^{-1} in the HSE regions from binary to ternary alloy. Cram et al. reported such

Table 2: The physical parameter values used in the kinetic model of Eq. 6, the dislocation-dislocation junction strength, α and activation energy for recovery, U_α were taken as fitting parameters.

Symbol	Parameter		Value	Unit	Reference
G	Shear modulus of α-Fe		77.5	GPa	[76]
M_{HSE}	Taylor factor		3.2		[77]
M_{LSE}			2.3		
α	dislocation-dislocation junction strength	binary	0.20 – 0.24		[16, 26]
		ternary	0.23 – 0.27		
$\mathbf{b}$	Burgers vector		$2.48 \cdot 10^{-10}$	m	[1]
U_α	Activation energy for recovery		245–290	$\mathrm{kJ\,mol^{-1}}$	[15, 16]
V_α	Activation volume for recovery		$12\mathbf{b}^3$	m^3	[60]
v_d	Debye frequency constant		$2 \cdot 10^{12}$	s^{-1}	[16]
E	Young modulus		200	GPa	

a behaviour with solute addition, as Sn solutes in Cu alloys increased α value from 0.2 in pure Cu to 0.3–0.35 by increasing solute content (0.2–5 wt.%) [13]. Meanwhile, in the LSE regions α remained the same for both samples (0.20).

Turning to *prior recovery*, DFXM results in Fig. 9c show the dislocation density decay in the individual grain B and T in comparison to the kinetic model. The DFXM data for the dislocation densities of the individual grains were fitted to the kinetic model by increasing the α from 0.2 to 0.23 with the addition of Sn, while U_α was kept constant at $245\,\mathrm{kJ\,mol^{-1}}$. The observed difference in the behaviour of the LSE regions from EBSD and DFXM may be due to the enhanced capabilities and angular resolution of DFXM or the higher available driving force for recovery (as experiments were performed below T_{REX}). The synchrotron data shows a good agreement with the microscopic measurements, even though it regards individual grain measurements and thus there is a certain degree of locality in the experiment.

For both alloys, the model agrees well with the values of dislocation density obtained experimentally. Generally, due to the higher dislocation density, α is higher in the HSE regions for both alloys. It was observed that solute addition had a stronger effect in the dislocation decay of HSE presumably due to solute impeding dislocation motion. Such an effect is remarkably higher in the regions of higher dislocation density. Effectively, in the presence of solute in HSE regions, dislocation motion is completely stalled. In parallel, the recovery concurrent to recrystallisation in LSE regions seems to be less affected as observed by the EBSD data showing a negligible solute effect. The present data suggest that the solute effect is weaker in the LSE regions – a reasonable observation as recovery processes could be expected to be more sluggish as stored energy decreases. Consequently, in the ternary alloy the difference in dislocation density consumption rate within the HSE and LSE regions during recovery is minimized (Fig. 9b). The present kinetic model, proposed by [15, 16], could explain reasonably well the recovery kinetics at the various length scales that were studied here and after partitioning the microstructure into zones of HSE and LSE.

5. Conclusion

The present study investigated the solute Sn effect during static recovery in single-phase ferritic Fe model alloys. The recovery phenomenon was studied comprehensively at various length scales using micro hardness, EBSD, and DFXM. The comparison of the experimental data to a physical kinetic model, suggest a strong evidence of solute-dislocation interaction during the recovery (prior and concurrent to recrystallisation) as the ternary alloy showed limited softening. The solute effect resulted in an increase in the dislocation-dislocation junction strength α constant, which was more pronounced in the high-stored energy (i.e. high Taylor factor) orientations. These observations could be attributed to Sn hindering – pinning – dislocation motion, an effect which was evident in both prior and concurrent recovery and at various temperatures. The solute-dislocation interaction was further discussed by the use of atomistic modelling results that demonstrated solute atmospheres around edge dislocations. The *in situ* recovery observations with DFXM were generally in accordance with the microscopic observations, although they were performed in relatively low stored energy regions. DFXM results were argued to provide a direct observation of a line dislocation intersecting a loop. The experimentally obtained (partial) sequence of such interaction could be rationalised with established ideas from the literature concerning the behaviour of dislocation intersections affected by solute adsorption. These results illustrate the capabilities of DFXM in grain-resolved studies and opens up new avenues even for highly-strained polycrystalline materials. Work in this direction is in progress.

Acknowledgements

N.Mavrikakis is grateful for the project supported by the National Association of Research and Technology (ANRT — Project no.1073–2015). C. Yildirim acknowledges H. Simons and S. Ahl for stimulating discussions notably on data analysis, and thanks Ayça Sönmez for graphical support. Finally, the authors acknowledge the ESRF for provision of beamtime on ID06.

References

[1] F. J. Humphreys, M. Hatherly, Recrystallization And Related Annealing Phenomena, 2nd Edition, Elsevier, 2004. `doi:10.1016/B978-0-08-044164-1.X5000-2`.

[2] R. D. Doherty, D. A. Hughes, F. J. Humphreys, J. J. Jonas, D. Juul Jensen, M. E. Kassner, W. E. King, T. R. McNelley, H. J. McQueen, A. D. Rollett,

Current issues in recrystallization: A review, Materials Today 1 (2) (1998) 14–15. `doi:10.1016/S1369-7021(98)80046-1`.

[3] A. H. Cottrell, Theory of dislocations, Progress in Metal Physics 4 (1953) 205–264. `doi:10.1016/0502-8205(53)90018-5`.

[4] P. C. J. Gallagher, The influence of alloying, temperature, and related effects on the stacking fault energy, Metallurgical Transactions A 1 (1967) 2429–2461. `doi:10.1007/BF03038370`.

[5] Y. Qi, R. K. Mishra, Ab initio study of the effect of solute atoms on the stacking fault energy in aluminum, Physical Review B 75 (22) (2007) 224105. `doi:10.1103/PhysRevB.75.224105`.

[6] K. Edalati, D. Akama, A. Nishio, S. Lee, Y. Yonenaga, J. M. Cubero-Sesin, Z. Horita, Influence of dislocation–solute atom interactions and stacking fault energy on grain size of single-phase alloys after severe plastic deformation using high-pressure torsion, Acta Materialia 69 (2014) 68–77. `doi:10.1016/j.actamat.2014.01.036`.

[7] G. Lyudkovsky, P. K. Rastogi, M. Bala, Nonoriented Electrical Steels, Journal of Metals 38 (1) (1986) 18–26.

[8] W. C. Leslie, Iron and its dilute substitutional solid solutions, Metallurgical Transactions 3 (1) (1972) 5–26. `doi:10.1007/bf02680580`.

[9] O. Kubaschewski, Iron-Binary phase diagrams, Springer, 1982. `doi:10.1007/978-3-662-08024-5`.

[10] H. J. McQueen, The production and utility of recovered dislocation substructures, Metallurgical Transactions A 8 (6) (1977) 807–824. `doi:10.1007/BF02661562`.

[11] G. Graiss, G. Saad, A. Fawzy, M. A. Kenawy, The effect of Sn segregation at grain boundary on the steady-state creep of Cu-10 wt% Sn alloy, Czechoslovak Journal of Physics 41 (2) (1991) 149–156. `doi:10.1007/BF01598134`.

[12] A. Varschavsky, E. Donoso, A calorimetric investigation on the kinetics of solute segregation to partial dislocations in Cu-3.34at%Sn, Materials Science and Engineering: A 251 (1-2) (1998) 208–215. `doi:10.1016/S0921-5093(98)00616-9`.

[13] D. G. Cram, X. Y. Fang, H. S. Zurob, Y. J. M. Bréchet, C. R. Hutchinson, The effect of solute on discontinuous dynamic recrystallization, Acta Materialia 60 (18) (2012) 6390–6404. `doi:10.1016/j.actamat.2012.08.021`.

[14] S. G. Song, J. S. Vetrano, S. M. Bruemmer, Pinning effect of solute atoms on grain boundary dislocation dissociation, Materials Science and Engineering: A 232 (1-2) (1997) 23–30. `doi:10.1016/S0921-5093(97)00090-7`.

[15] M. Verdier, Y. Brechet, P. Guyot, Recovery of AlMg alloys: flow stress and strain-hardening properties, Acta Materialia 47 (1) (1998) 127–134. `doi:10.1016/S1359-6454(98)00350-4`.

[16] H. S. Zurob, C. R. Hutchinson, Y. Brechet, G. Purdy, Modeling recrystallization of microalloyed austenite: effect of coupling recovery, precipitation and recrystallization, Acta Materialia 50 (12) (2002) 3077–3094. `doi:10.1016/S1359-6454(02)00097-6`.

[17] H. Simons, A. King, W. Ludwig, C. Detlefs, W. Pantleon, S. Schmidt, F. Stöhr, I. Snigireva, A. Snigirev, H. F. Poulsen, Dark-field X-ray microscopy for multiscale structural characterization, Nature Communications 6 (1) (2015) 6098. `doi:10.1038/ncomms7098`.

[18] G. Winther, X. Huang, A. Godfrey, N. Hansen, Critical comparison of dislocation boundary alignment studied by TEM and EBSD: technical issues and theoretical consequences, Acta Materialia 52 (15) (2004) 4437–4446. `doi:10.1016/j.actamat.2004.05.050`.

[19] S. R. Ahl, H. Simons, Y. Zhang, C. Detlefs, F. Stöhr, A. C. Jakobsen, D. J. Jensen, H. F. Poulsen, Ultra-low-angle boundary networks within recrystallizing grains, Scripta Materialia 139 (2017) 87–91.

[20] H. F. Poulsen, A. C. Jakobsen, H. Simons, S. R. Ahl, P. K. Cook, C. Detlefs, X-ray diffraction microscopy based on refractive optics, Journal of Applied Crystallography 50 (5) (2017) 1441–1456. `doi:10.1107/S1600576717011037`.

[21] S. Schmidt, S. F. Nielsen, C. Gundlach, L. Margulies, X. Huang, D. J. Jensen, Watching the growth of bulk grains during recrystallization of deformed metals, Science 305 (5681) (2004) 229–232. `arXiv:http://science.sciencemag.org/content/305/5681/229.full.pdf`, `doi:10.1126/science.1098627`.
URL `http://science.sciencemag.org/content/305/5681/229`

[22] J. Sun, T. Yu, C. Xu, W. Ludwig, Y. Zhang, 3d characterization of partially recrystallized al using high resolution diffraction contrast tomography, Scripta Materialia 157 (2018) 72–75.

[23] O. Kapikranian, H. Zapolsky, C. Domain, R. Patte, C. Pareige, B. Radiguet, P. Pareige, Atomic structure of grain boundaries in iron modeled using the atomic density function, Physical Review B 89 (1) (2014) 014111. `doi:10.1103/PhysRevB.89.014111`.

[24] M. Lavrskyi, H. Zapolsky, A. G. Khachaturyan, Quasiparticle approach to diffusional atomic scale self-assembly of complex structures: from disorder to complex crystals and double-helix polymers, npj Computational Materials 2 (1) (2016) 15013. `doi:10.1038/npjcompumats.2015.13`.

[25] D. A. Hughes, N. Hansen, Microstructure and strength of nickel at large strains, Acta Materialia 48 (11) (2000) 2985–3004. `doi:10.1016/S1359-6454(00)00082-3`.

[26] S. S. Hazra, A. A. Gazder, E. V. Pereloma, Stored energy of a severely deformed interstitial free steel, Materials Science and Engineering: A 524 (1-2) (2009) 158–167. `doi:10.1016/j.msea.2009.06.033`.

[27] W. Q. Cao, C. F. Gu, E. V. Pereloma, C. H. J. Davies, Stored energy, vacancies and thermal stability of ultra-fine grained copper, Materials Science and Engineering: A 492 (1-2) (2008) 74–79. `doi:10.1016/j.msea.2008.02.048`.

[28] J. A. Muñoz, O. F. Higuera, A. H. Expósito, A. Boulaajaj, R. E. Bolmaro, F. D. Dumitru, P. R. Calvillo, A. M. Jorge, J. M. Cabrera, Thermal stability of ARMCO iron processed by ECAP, The International Journal of Advanced Manufacturing Technology 98 (9-12) (2018) 2917–2932. `doi:10.1007/s00170-018-2353-7`.

[29] H. J. Bunge, Texture Analysis in Materials Science, Butterworth-Heinemann, 1969.

[30] D. Griffiths, J. N. Riley, Dislocation arrangements in deformed polycrystalline 3% silicon-iron, Acta Metallurgica 14 (6) (1966) 755–773. `doi:10.1016/0001-6160(66)90123-4`.

[31] I. L. Dillamore, C. J. E. Smith, T. W. Watson, Oriented nucleation in the formation of annealing textures in iron, Metal Science Journal 1 (1) (1967) 49–54. `doi:10.1179/msc.1967.1.1.49`.

[32] B. Hutchinson, Deformation microstructures and textures in steels, Philosophical Transactions of the Royal Society A: Mathematical, Physical and Engineering Sciences 357 (1756) (1999) 1471–1485. `doi:10.1098/rsta.1999.0385`.

[33] I. L. Dillamore, J. G. Roberts, A. C. Bush, Occurrence of shear bands in heavily rolled cubic metals, Metal Science 13 (2) (1979) 73–77. `doi:10.1179/msc.1979.13.2.73`.

[34] W. B. Hutchinson, Development and control of annealing textures in low-carbon steels, International Metals Reviews 29 (1) (1984) 25–42. `doi:10.1179/imtr.1984.29.1.25`.

[35] M. Z. Quadir, B. J. Duggan, Deformation banding and recrystallization of α fibre components in heavily rolled IF steel, Acta Materialia 52 (13) (2004) 4011–4021. `doi:10.1016/j.actamat.2004.05.017`.

[36] H. Inagaki, Fundamental Aspect of Texture Formation in Low Carbon Steel., ISIJ International 34 (4) (1994) 313–321. `doi:10.2355/isijinternational.34.313`.

[37] M. Hoelscher, D. Raabe, K. Luecke, Rolling and recrystallization textures of bcc steels, Steel Res 62 (12) (1991) 567–575.

[38] P. N. Kalu, D. R. Waryoba, A JMAK-microhardness model for quantifying the kinetics of restoration mechanisms in inhomogeneous microstructure, Materials Science and Engineering: A 464 (1-2) (2007) 68–75. `doi:10.1016/j.msea.2007.01.124`.

[39] J. T. Busby, M. C. Hash, G. S. Was, The relationship between hardness and yield stress in irradiated austenitic and ferritic steels, Journal of Nuclear Materials 336 (2-3) (2005) 267–278. `doi:10.1016/j.jnucmat.2004.09.024`.

[40] G. Saada, Sur le durcissement dû à la recombinaison des dislocations, Acta Metallurgica 8 (12) (1960) 841–847. `doi:10.1016/0001-6160(60)90150-4`.

[41] U. F. Kocks, H. Mecking, Physics and phenomenology of strain hardening: the FCC case, Progress in Materials Science 48 (3) (2003) 171–273. `doi:10.1016/S0079-6425(02)00003-8`.

[42] J. Friedel, Dislocations, Pergamon Press, Oxford, 1964.

[43] D. Kuhlmann, G. Masing, J. Raffelsieper, Zur Theorie Der Erholung, Zeitschrift fur Metallkunde 40 (1949) 241–246.

[44] S. R. Ahl, Elements of a Method for Multiscale Characterization of Recrystallization in Deformed Metals, Ph.D. thesis, Technical University of Denmark (2018).

[45] O. Kapikranian, H. Zapolsky, R. Patte, C. Pareige, B. Radiguet, P. Pareige, Point defect absorption by grain boundaries inα-iron by atomic density

function modeling, Physical Review B 92 (22) (2015) 224106. doi:10.1103/PhysRevB.92.224106.

[46] Y. M. Jin, A. G. Khachaturyan, Atomic density function theory and modeling of microstructure evolution at the atomic scale, Journal of Applied Physics 100 (1) (2006) 013519. doi:10.1063/1.2213353.

[47] A. Stukowski, K. Albe, Extracting dislocations and non-dislocation crystal defects from atomistic simulation data, Modelling and Simulation in Materials Science and Engineering 18 (8) (2010) 085001. doi:10.1088/0965-0393/18/8/085001.

[48] A. Stukowski, V. V. Bulatov, A. Arsenlis, Automated identification and indexing of dislocations in crystal interfaces, Modelling and Simulation in Materials Science and Engineering 20 (8) (2012) 085007. doi:10.1088/0965-0393/20/8/085007.

[49] A. H. Cottrell, B. A. Bilby, Dislocation Theory of Yielding and Strain Ageing of Iron, Proceedings of the Physical Society. Section A 62 (1) (1949) 49–62. doi:10.1088/0370-1298/62/1/308.

[50] E. Nes, Recovery revisited, Acta Metallurgica et Materialia 43 (6) (1995) 2189–2207. doi:10.1016/0956-7151(94)00409-9.

[51] J. W. Cahn, The impurity drag effect in grain boundary motion, Acta Metallurgica 10 (9) (1962) 789–798. doi:10.1016/0001-6160(62)90092-5.

[52] K. Tapasa, D. J. Bacon, Y. N. Osetsky, Simulation of dislocation glide in dilute Fe – Cu alloys, Materials Science and Engineering: A 400-401 (2005) 109–113. doi:10.1016/j.msea.2005.03.057.

[53] M. I. Pascuet, E. Martínez, G. Monnet, L. Malerba, Solute effects on edge dislocation pinning in complex alpha-Fe alloys, Journal of Nuclear Materials 494 (2017) 311–321. doi:10.1016/j.jnucmat.2017.07.049.

[54] C. Domain, C. S. Becquart, Solute - $\langle 111 \rangle$ interstitial loop interaction in α-Fe: A DFT study, Journal of Nuclear Materials 499 (2018) 582–594. doi:10.1016/j.jnucmat.2017.10.070.

[55] S. F. Antani, P. G. Klemens, Formation of solute atmospheres around dislocations, Physical Review B 11 (8) (1975) 2771–2776. doi:10.1103/PhysRevB.11.2771.

[56] N. Louat, On stress relaxation in dislocation solute atmospheres, Philosophical Magazine A 44 (1) (1981) 223–228. doi:10.1080/01418618108244503.

[57] S. Takeuchi, A. S. Argon, Steady-state creep of alloys due to viscous motion of dislocations, Acta Metallurgica 24 (10) (1976) 883–889. doi:10.1016/0001-6160(76)90036-5.

[58] F. R. N. Nabarro, Distribution of solute atoms round a moving dislocation, Materials Science and Engineering: A 400-401 (2005) 22–24. doi:10.1016/j.msea.2005.03.046.

[59] Y. Hanlumyuang, P. A. Gordon, T. Neeraj, D. C. Chrzan, Interactions between carbon solutes and dislocations in bcc iron, Acta Materialia 58 (16) (2010) 5481–5490. doi:10.1016/j.actamat.2010.06.024.

[60] F. G. Arieta, C. M. Sellars, Activation volume and activation energy for deformation of Nb HSLA steels, Scripta Metallurgica et Materialia 30 (6) (1994) 707–712. doi:10.1016/0956-716X(94)90186-4.

[61] R. Kirchheim, Reducing grain boundary, dislocation line and vacancy formation energies by solute segregation. I. Theoretical background, Acta Materialia 55 (15) (2007) 5129–5138. doi:10.1016/j.actamat.2007.05.047.

[62] D. Blavette, Three-Dimensional Atomic-Scale Imaging of Impurity Segregation to Line Defects, Science 286 (5448) (1999) 2317–2319. doi:10.1126/science.286.5448.2317.

[63] J. Takahashi, K. Kawakami, J.-i. Hamada, K. Kimura, Direct observation of niobium segregation to dislocations in steel, Acta Materialia 107 (2016) 415–422. doi:10.1016/j.actamat.2016.01.070.

[64] G. Da Rosa, P. Maugis, J. Drillet, V. Hebert, K. Hoummada, Co-segregation of boron and carbon atoms at dislocations in steel, Journal of Alloys and Compounds 724 (2017) 1143–1148. doi:10.1016/j.jallcom.2017.07.096.

[65] M. Hatakeyama, S. Tamura, I. Yamagata, Direct observation of solute–dislocation interaction on screw dislocation in a neutron irradiated modified 316 stainless steel, Materials Letters 122 (2014) 301–305. doi:10.1016/j.matlet.2014.01.109.

[66] A. Jakobsen, H. Simons, W. Ludwig, H. Leemreize, L. Porz, C. Detlefs, H. Poulsen, Mapping of individual dislocations with dark field x-ray microscopy, Journal of Applied Crystallography in print.

[67] D. Hull, D. J. Bacon, Introduction to Dislocations, Elsevier, 2011. doi:10.1016/C2009-0-64358-0.

[68] D. Terentyev, F. Bergner, Y. Osetsky, Cr segregation on dislocation loops enhances hardening in ferritic Fe – Cr alloys, Acta Materialia 61 (5) (2013) 1444–1453. doi:10.1016/j.actamat.2012.11.021.

[69] B. C. Masters, Dislocation loops in irradiated iron, Philosophical Magazine 11 (113) (1965) 881–893. doi:10.1080/14786436508223952.

[70] R. P. Wei, A. J. Baker, Observation of dislocation loop arrays in fatigued polycrystalline pure iron, Philosophical Magazine 11 (113) (1965) 1087–1091. doi:10.1080/14786436508223967.

[71] A. Gemperle, M. Rozsíval, B. Šesták, Electron microscope study of dislocations in slip bands of bent Fe-3.2% Si alloy single crystals, Czechoslovak Journal of Physics 12 (7) (1962) 555–560. doi:10.1007/BF01689438.

[72] D. Terentyev, X. He, G. Bonny, A. Bakaev, E. Zhurkin, L. Malerba, Hardening due to dislocation loop damage in RPV model alloys: Role of Mn segregation, Journal of Nuclear Materials 457 (2015) 173–181. doi:10.1016/j.jnucmat.2014.11.023.

[73] B. D. Wirth, G. R. Odette, D. Maroudas, G. E. Lucas, Dislocation loop structure, energy and mobility of self-interstitial atom clusters in bcc iron, Journal of Nuclear Materials 276 (1-3) (2000) 33–40. doi:10.1016/S0022-3115(99)00166-X.

[74] R. G. Faulkner, S.-H. Song, P. E. J. Flewitt, Determination of impurity–point defect binding energies in alloys, Materials Science and Technology 12 (11) (1996) 904–910. doi:10.1179/mst.1996.12.11.904.

[75] D. Terentyev, N. Anento, A. Serra, V. Jansson, H. Khater, G. Bonny, Interaction of carbon with vacancy and self-interstitial atom clusters in α-iron studied using metallic–covalent interatomic potential, Journal of Nuclear Materials 408 (3) (2011) 272–284. doi:10.1016/j.jnucmat.2010.11.053.

[76] N. Hansen, Boundary strengthening in undeformed and deformed polycrystals, Materials Science and Engineering: A 409 (1-2) (2005) 39–45. doi:10.1016/j.msea.2005.04.061.

[77] A. A. Gazder, F. D. Torre, C. F. Gu, C. H. J. Davies, E. V. Pereloma, Microstructure and texture evolution of bcc and fcc metals subjected to equal channel angular extrusion, Materials Science and Engineering: A 415 (1-2) (2006) 126–139. doi:10.1016/j.msea.2005.09.065.

[78] M. Bellavoine, M. Dumont, J. Drillet, V. Hébert, P. Maugis, Combined Effect of Heating Rate and Microalloying Elements on Recrystallization During Annealing of Dual-Phase Steels, Metallurgical and Materials Transactions A 49 (7) (2018) 2865–2875. doi:10.1007/s11661-018-4642-z.